# Experimentally-constrained biophysical models of tonic and burst firing modes in thalamocortical neurons

Elisabetta Iavarone[1*], Jane Yi[2], Ying Shi[1,2], Bas-Jan Zandt[1], Christian O'Reilly[1], Werner Van Geit[1], Christian A. Rössert[1], Henry Markram[1,2], and Sean L. Hill[1,3]

[1]Blue Brain Project, École polytechnique fédérale de Lausanne (EPFL), Geneva, Switzerland

[2]Laboratory of Neural Microcircuitry (LNMC), École polytechnique fédérale de Lausanne (EPFL) (EPFL), Lausanne, Switzerland

[3]Krembil Centre for Neuroinformatics, CAMH, Toronto, Canada

* Corresponding author

E-mail: elisabetta.iavarone@epfl.ch

## Abstract

Somatosensory thalamocortical (TC) neurons from the ventrobasal (VB) thalamus are central components in the flow of sensory information between the periphery and the cerebral cortex, and participate in the dynamic regulation of thalamocortical states including wakefulness and sleep. This property is reflected at the cellular level by the ability to generate action potentials in two distinct firing modes, called tonic firing and low-threshold bursting. Although the general properties of TC neurons are known, we still lack a detailed characterization of their morphological and electrical properties in the VB thalamus. The aim of this study was to build biophysically-detailed models of VB TC neurons explicitly constrained with experimental data from rats. We recorded the electrical activity of VB neurons (N = 49) and reconstructed morphologies in 3D (N = 50) by applying standardized protocols. After identifying distinct electrical types, we used a multi-objective optimization to fit single neuron electrical models (e-models), which yielded multiple solutions consistent with the experimental data. The models were tested for generalization using electrical stimuli and neuron morphologies not used during fitting. A local sensitivity analysis revealed that the e-models are robust to small parameter changes and that all the parameters were constrained by one or more features. The e-models, when tested in combination with different morphologies, showed that the electrical behavior is substantially preserved when changing dendritic structure and that the e-models were not overfit to a specific morphology. The models and their analysis show that automatic parameter search can be applied to capture complex firing behavior, such as co-existence of tonic firing

and low-threshold bursting over a wide range of parameter sets and in combination with different neuron morphologies.

## Author summary

Thalamocortical neurons are one of the main components of the thalamocortical system, which are implicated in key functions including sensory transmission and the transition between brain states. These functions are reflected at the cellular level by the ability to generate action potentials in two distinct modes, called burst and tonic firing. Biophysically-detailed computational modeling of these cells can provide a tool to understand the role of these neurons within thalamocortical circuitry. We started by collecting single cell experimental data by applying standardized experimental procedures in brain slices of the rat. Prior work has demonstrated that biological constraints can be integrated using multi-objective optimization to build biologically realistic models of neuron. Here, we employ similar techniques as those previously employed, but extend them to capture the multiple firing modes of thalamic neurons. We compared the model results with additional experimental data test their generalization and quantitatively reject those that deviated significantly from the experimental variability. These models can be readily integrated in a data-driven pipeline to reconstruct and simulate circuit activity in the thalamocortical system.

## Introduction

Thalamocortical (TC) neurons are one of the main components of the thalamus and have been extensively studied *in vitro* and *in computo*, especially in first order thalamic nuclei in different species (1). One of these nuclei, namely the ventral posterolateral nucleus (VPL), relays somatosensory, proprioceptive, and nociceptive information from the whole body to the somatosensory (non-barrel) cortex (2). The VPL is located close to ventral posteromedial nucleus (VPM), which transmits information from the face to the barrel cortex. The VPL and VPM nuclei constitute the ventrobasal (VB) complex of the thalamus (3).

Despite its key role in sensory functions, a systematic characterization of the cellular properties of the VB complex is still missing. The morphologies of VPL neurons in adult rats were described in early anatomical studies but were limited to two-dimensional drawings of Golgi-impregnated cells (4). The general electrical properties of TC neurons maintained *in vitro* are known and similar in different thalamic nuclei and species with respect to the generation of two distinct firing modes, called tonic firing and low-threshold bursting (5–8). However, a systematic description on the electrical types in the VB thalamus in the rodents is still missing.

Collecting morphological and electrophysiological data, by following standardized experimental procedures, is essential for the definition of cells types and it is the first step to constraining computational models of single neurons (9,10). Although models of TC neurons have already been previously published, they typically were aimed at studying specific firing properties and their parameters were hand tuned to achieve the desired result (11–15).

The purpose of our study is to systematically define the morphological and electrical types by collecting *in vitro* experimental data and to constrain biophysically detailed models of

78 VB TC neurons of the juvenile rat. To the best of our knowledge, automatic parameter search
79 has not been applied, thus far, to capture complex firing behavior in thalamic neurons, in
80 particular low-threshold bursting and tonic firing. We defined the electrical and morphological
81 types of TC neurons through in vitro patch-clamp recordings and 3D morphological
82 reconstructions. We then extended an existing method (16) to account for their distinctive
83 firing properties. These electrical models (e-models) were constrained by the electrical features
84 extracted from experimental data (9,17,18). Other experimental data were used to assess the
85 generalization of the models to different stimuli and morphologies. We further performed a
86 sensitivity analysis by varying each parameter at a time by a small amount and recording the
87 resulting electrical features. This analysis provides an assessment of the robustness of the
88 models and a verification that the selected features provide sufficient constraints for the
89 parameters.

## 90 Results

### 91 Physiological and morphological characterization

92 We characterized TC neurons in slices of the rat VB thalamus, by combining whole-cell patch-
93 clamp recordings, biocytin filling and 3D Neurolucida (MicroBrightField) reconstruction, along
94 with anatomical localization in a reference atlas (19) (Fig 1).
95

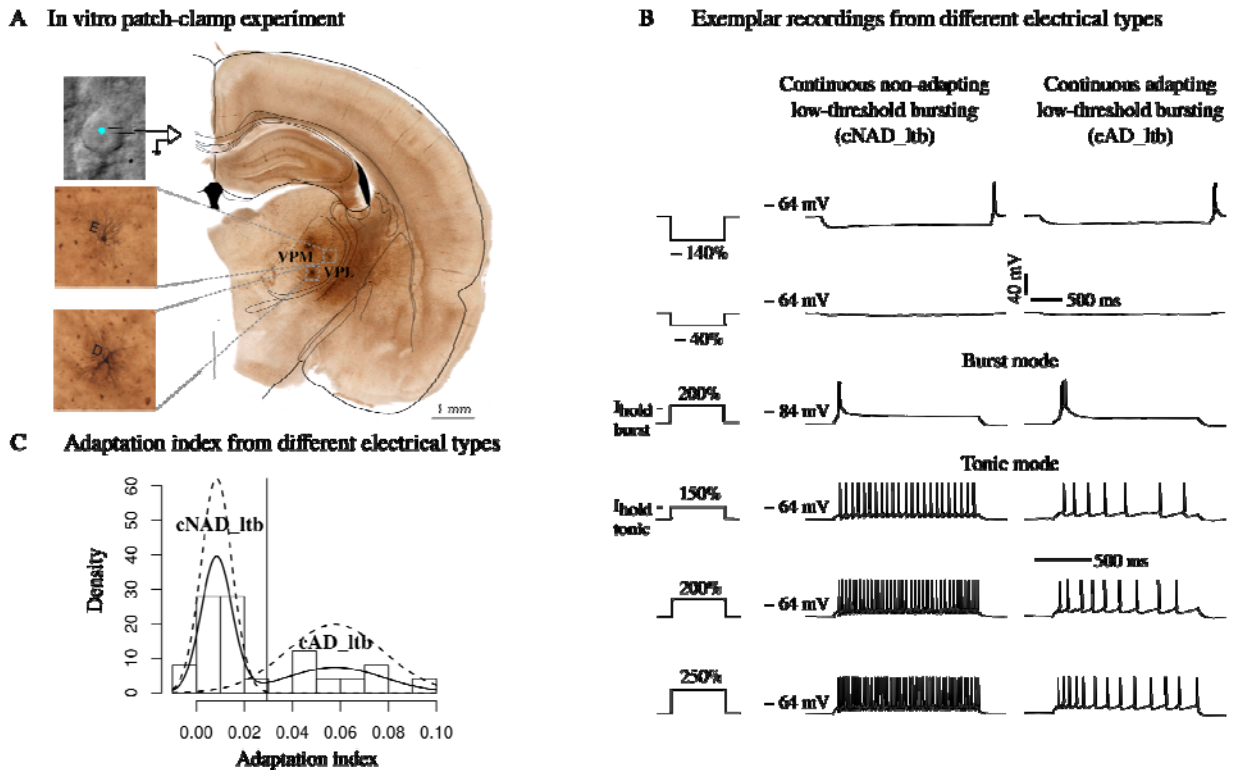


**Figure 1: Simultaneous physiological and morphological characterization.**

(A) View of a patched cell under optic microscope and anatomical localization of biocytin-filled neurons (insets) in the rat Paxinos and Watson atlas (19). Letters D and E identify morphologies in a slice. (B) Voltage responses of two different thalamocortical (TC) neurons to a standardized battery of current stimuli. Each current amplitude was normalized by the threshold current of each neuron (e.g. 150 % threshold, see Methods). Third row is a low-threshold burst response from a hyperpolarized holding potential, $V_{hold}$ = −84 mV (burst mode), the other responses are elicited from a depolarized holding potential, $V_{hold}$ = −64 mV (tonic mode). Two different holding currents ($I_{hold}$ - tonic, $I_{hold}$ - burst) are injected to obtain the desired $V_{hold}$. The vertical scale bar applies to all the traces, the first horizontal scale bar from the top refers to the first two rows, the second applies to the last four rows. (C) Analysis of adaptation index (AI) from

recordings in tonic mode. Solid line is a non-parametric estimation of the distribution, dashed lines are two Gaussian distributions fitted to the data (see Methods). The vertical line indicates the cut-off value.

Visual inspection of 50 reconstructed morphologies (24 from the VPL, 26 from the VPM nuclei) revealed variability in the number of principal dendritic trunks and their orientation, in agreement with previous anatomical studies (4).

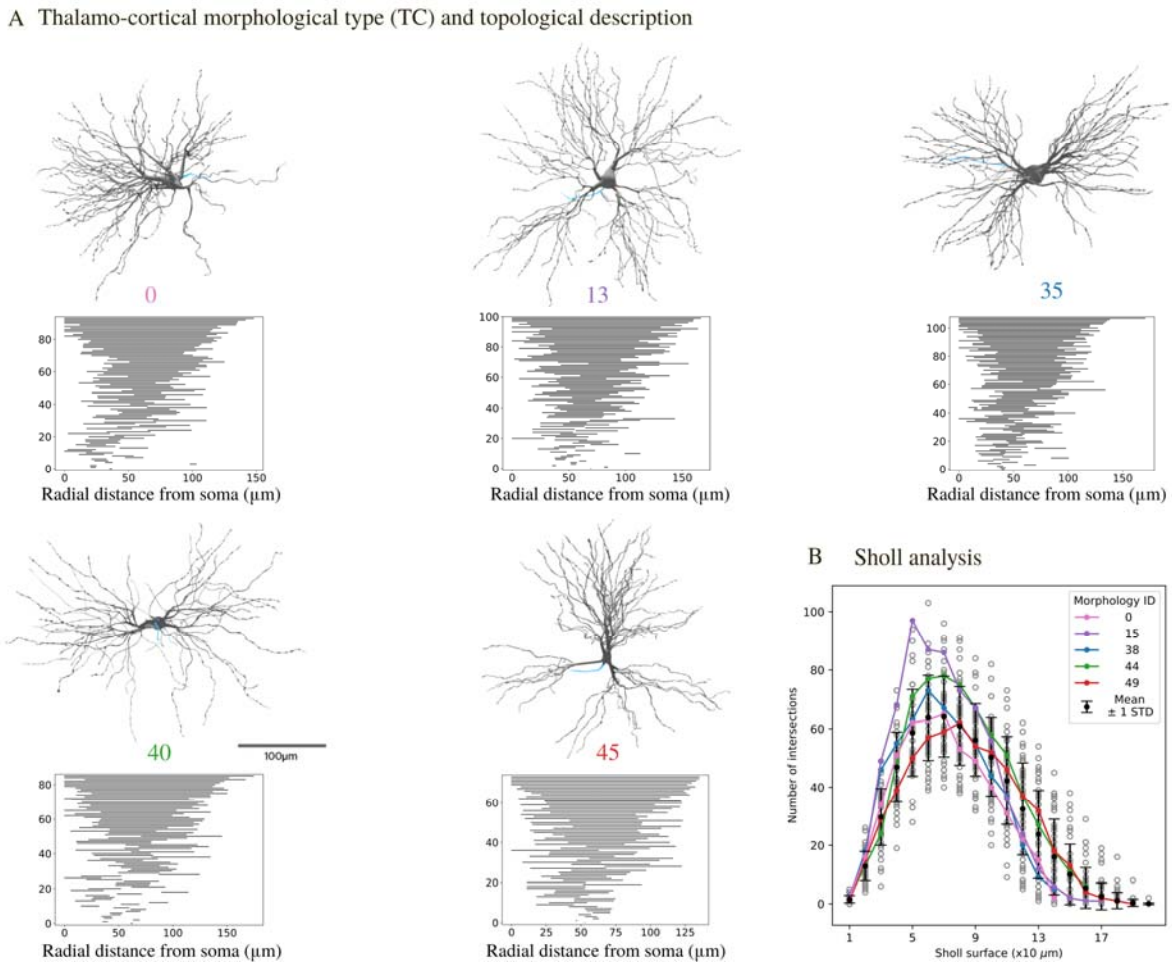


**Figure 2: Morphological properties.**

119 (A) Renderings of 3D reconstructed TC neurons along with their persistence barcode according
120 to (20). Grey: soma and dendrites, blue: axon only small sections available). The persistence
121 barcode is a topological description of the branching pattern of the neurons' dendrites. (B) Sholl
122 analysis of TC neuron dendrites. For each Sholl ring, the number of intersections is shown
123 (mean ± standard deviation, N = 50). Each grey circle represents one morphology, colored lines
124 correspond to the morphologies in A. See Fig S1 for further analysis.
125
126 The maximum radial extent of the dendrites ranged between 120 and 200 µm and they
127 started to branch between 20 and 50 µm from the soma (Fig S1). We then analyzed the
128 morphologies with two methods in order to quantitavely classify different morphological types.
129 We used algebraic topology to extract the persistent homology of each morphology and to
130 visualize the persistence barcode (20) (Fig 2A, see Methods). Each horizontal bar in the
131 persistence barcode represents the start and end point of each dendritic component in terms
132 of its radial distance from the soma. The barcodes of all the morphologies followed a semi-
133 continuous distribution of decreasing length. To quantify the differences between the
134 barcodes, we computed the pairwise distances of the persistence images (see Methods and Fig
135 S1). We found that they were in general small (<0.4, values expected to vary between 0 and 1).
136 These findings indicate that the morphologies cannot be grouped in different classes based on
137 the topology of their dendrites. Furthermore, we performed Sholl Analysis (21) to compare the
138 complexity of the dendritic trees (Fig 2B). We observed that all the morphologies had dense
139 dendritic branches, with a maximum number of 50-100 intersections between 50-80 µm from
140 the soma. When comparing the Sholl profiles for each pair of neurons we could not find any

141 statistically significant difference (Fig S1C). Considering the results of topological and Sholl
142 analyses, we grouped all the morphologies in one morphological type (m-type) called
143 thalamocortical (TC) m-type.

144 We used an adaptive stimulation protocol, called e-code, consisting of a battery of
145 current stimuli (e- code, see Methods for details), where the stimulation amplitude was
146 adapted to the excitability of different neurons. This standardized protocol has previously been
147 used to build biophysically-accurate models of cortical electrical types (e-types) (16). However,
148 TC neurons from different thalamic nuclei and species fire action potentials in two distinct firing
149 modes, namely tonic firing, when stimulated from a relatively depolarized membrane potential
150 or low-threshold bursting, from a hyperpolarized membrane potential (5). We thus extended
151 the e-code to include two different holding currents. All the neurons recorded in this study
152 displayed tonic and burst firing, when stimulated with the appropriate holding current (Fig 1).
153 Moreover, we were able to classify different e-types by considering the voltage traces recorded
154 in tonic mode in response to step current injections (Fig 1). The majority of the cells (59.3 %)
155 showed a non- adapting tonic discharge (continuous non-adapting low-threshold bursting,
156 cNAD_ltb e-type) while others (40.7 %) had higher adaptation rates (continuous non-adapting
157 low-threshold bursting, cAD_ltb e-type), as reflected by the adaptation index (Fig 1C). We
158 followed the Petilla convention (22) for naming the tonic firing discharge (cNAD or cAD),
159 extending it to include "_ltb" for the low-threshold bursting property. In some rare examples,
160 we noticed acceleration in the firing rate with decreasing inter-spike intervals (ISIs) towards the
161 end of the stimulus. Similar adapting and accelerating responses have already been described in
162 the VB thalamus of the cat (7). We also observed stereotypical burst firing responses within the

163 same cell, with variation of the number of spikes per burst in different cells, but the burst firing
164 responses alone were insufficient to classify distinct e-types.
165
166 **Constraining the models with experimental data**
167 Multi-compartmental models comes with the need of tuning a large number of
168 parameters (23), therefore we constrained the models as much as possible from experimental
169 data. We first combined the morphology and the ionic currents models in the different
170 morphological compartments (soma, dendrites and axon). Given that the reconstruction of the
171 axon was limited, we replaced it with a stub representing the initial segment (16). We used
172 previously published ionic current models and selected those that best matched properties
173 measured in rat TC neurons (see Methods). The kinetics parameters were not part of the free
174 parameters of the models. The distribution of the different ionic currents and their
175 conductances in the dendrites of TC neurons is largely unknown. The current amplitudes of the
176 fast sodium, persistent and transient (A-type) potassium currents were measured, but only up
177 to 40-50 µm from the soma (24). Indirect measures of burst properties (15) or $Ca^{2+}$ imaging
178 studies (25) suggest that the low-threshold calcium (T-type) channels are uniformly distributed
179 in the somatodendritic compartments. We thus assumed different peak conductance in the
180 soma, dendrites and axon for all the ionic currents, except for $I_{CaT}$, which had the same
181 conductance value in the soma and dendrites. We then extracted the mean and standard
182 deviation (STD) of different electrical features in order to capture the variability of firing
183 responses from different cells of the same e-type (9) (Fig 3).
184

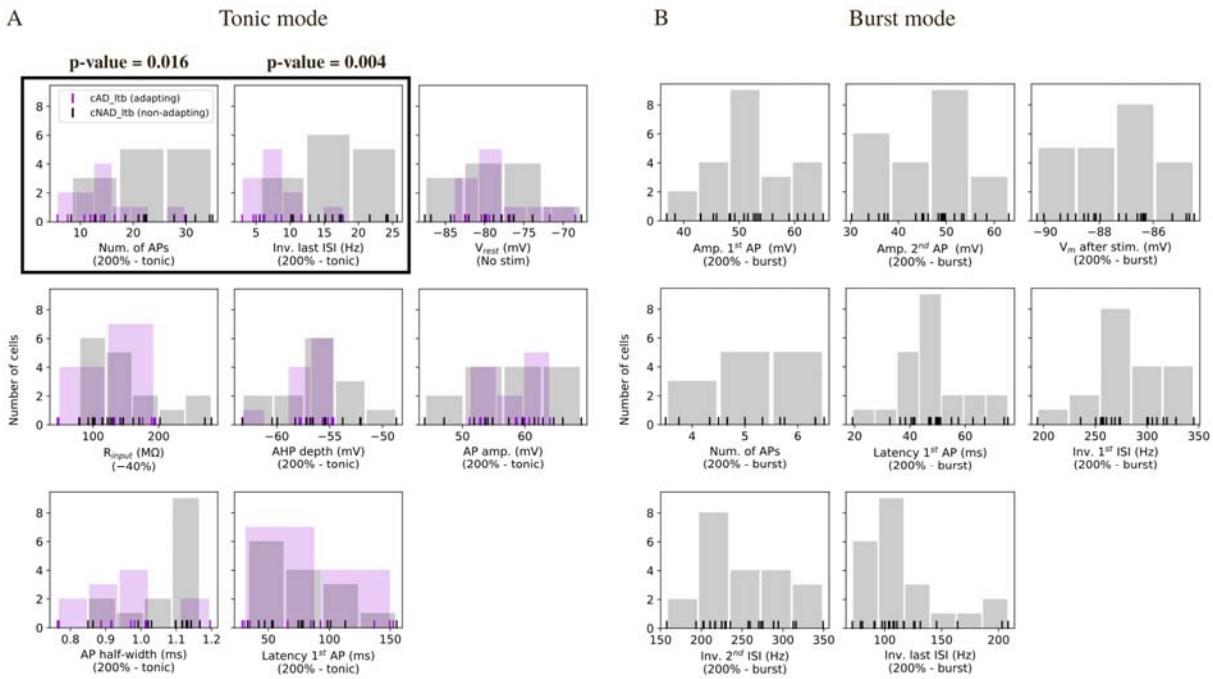


**Figure 3: Histograms of electrical features.**

Each vertical line represents the mean feature value for a cell. Tonic and burst refer to the holding voltage as in Fig 1. (A) Feature values extracted from recordings in tonic mode (N = 11 cAD_ltb cells, N = 16 cNAD_ltb cells). The features highlighted by a black box show different distributions for the cNAD_ltb and cAD_ltb electrical types (e-types) (p-value<0.05, two- sided Mann-Whitney U test with Bonferroni correction for multiple comparisons). Passive properties ($V_{rest}$, $R_{input}$) and spike shape features (AHP depth, AP amp., etc.) did not show clear differences between the two e-types. (B) Features measuring burst firing properties (N = 22 cells).

We observed that some features extracted from tonic firing responses had distinct distributions between the cAD_ltb and cNAD_ltb e-types (Fig 3A). The features were chosen in order to quantify salient physiological properties of TC neurons and to constrain the

parameters of the model, namely the peak conductance of each ionic current. The average value and STD of the features were used as optimization objective (multi-objective optimization, MOO). Twenty-five parameters were allowed to vary between the upper and lower bounds shown in Fig 5. The models were associated with a training error, i.e. a set of all the feature errors (measured as absolute z-scores) (9,18,26).

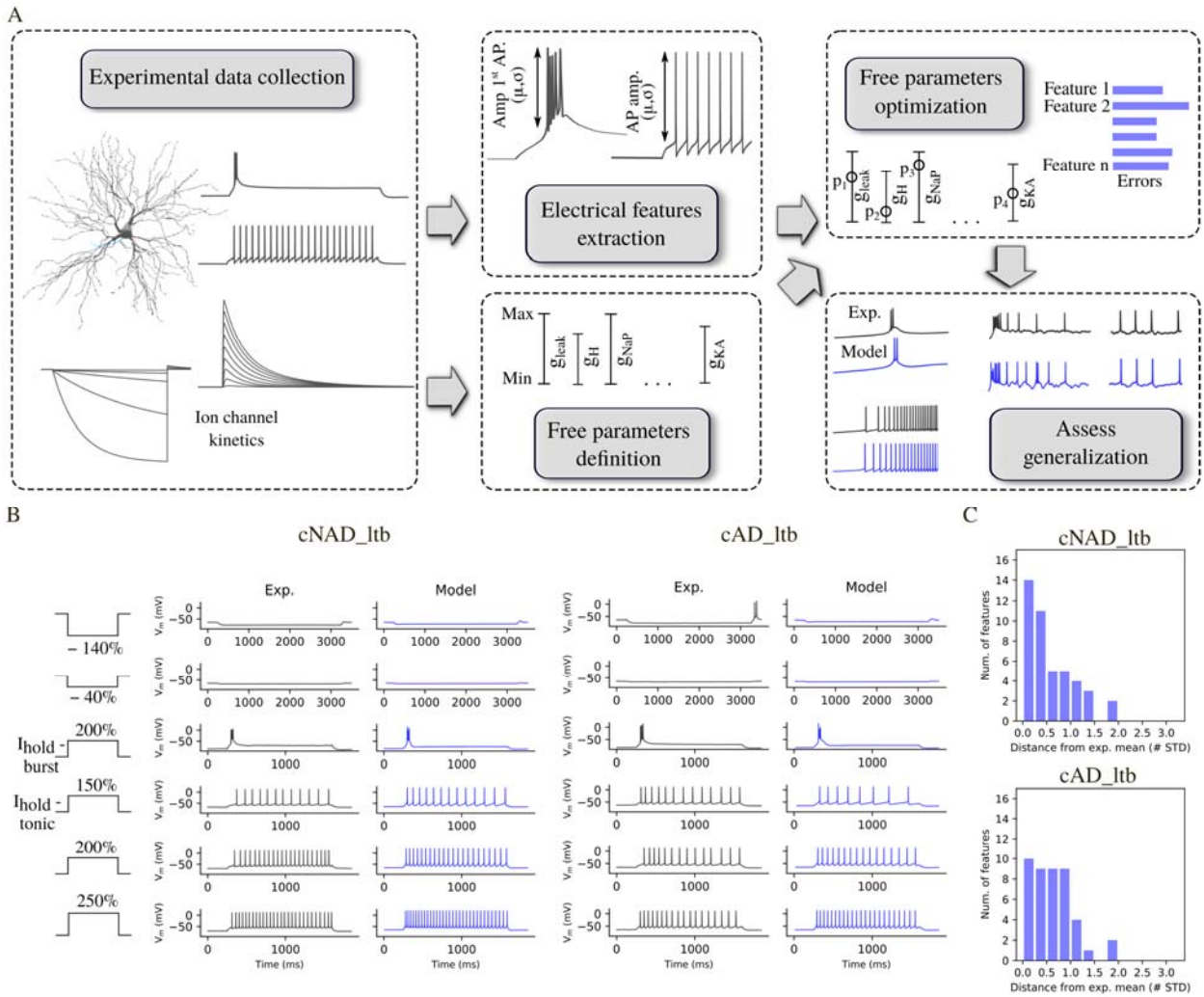


**Figure 4: Models of different TC e-types and their fitting errors.**

(A) Single neuron modelling pipeline. (B) Experimental and model voltage responses to a variety of stimuli pattern used during the optimization of cNAD_ltb and cAD_ltb e-types. (C) Feature errors of the models shown in (B) reported as deviation from the experimental mean. The

models are compared with the mean of features shown in Fig 3. Note that the models shown in B are fitted in order to reproduce the mean firing properties, not only a specific experimental recording. See Fig S2 for a complete list of fitting errors. By applying this MOO procedure, we generated multiple models with distinct parameter combinations that reproduced tonic and low-threshold burst firing in cNAD_ltb and cAD_ltb e-types (Fig 4).

**Model and experimental diversity**

We found that different sets of parameter values reproduced the target firing behavior (Fig 5B). We further analyzed models that had all the feature errors below 3 STD. Models' voltage responses reflected the characteristic firing properties of TC neurons (Fig S3), indicating that the selected set of features were sufficient to capture the two firing modes, in both the adapting and non-adapting e-types. The voltage traces from different models showed small differences in spike amplitude, firing frequency, and depth of the after-hyperpolarization, as reflected by the variability of features values (Fig 5C).

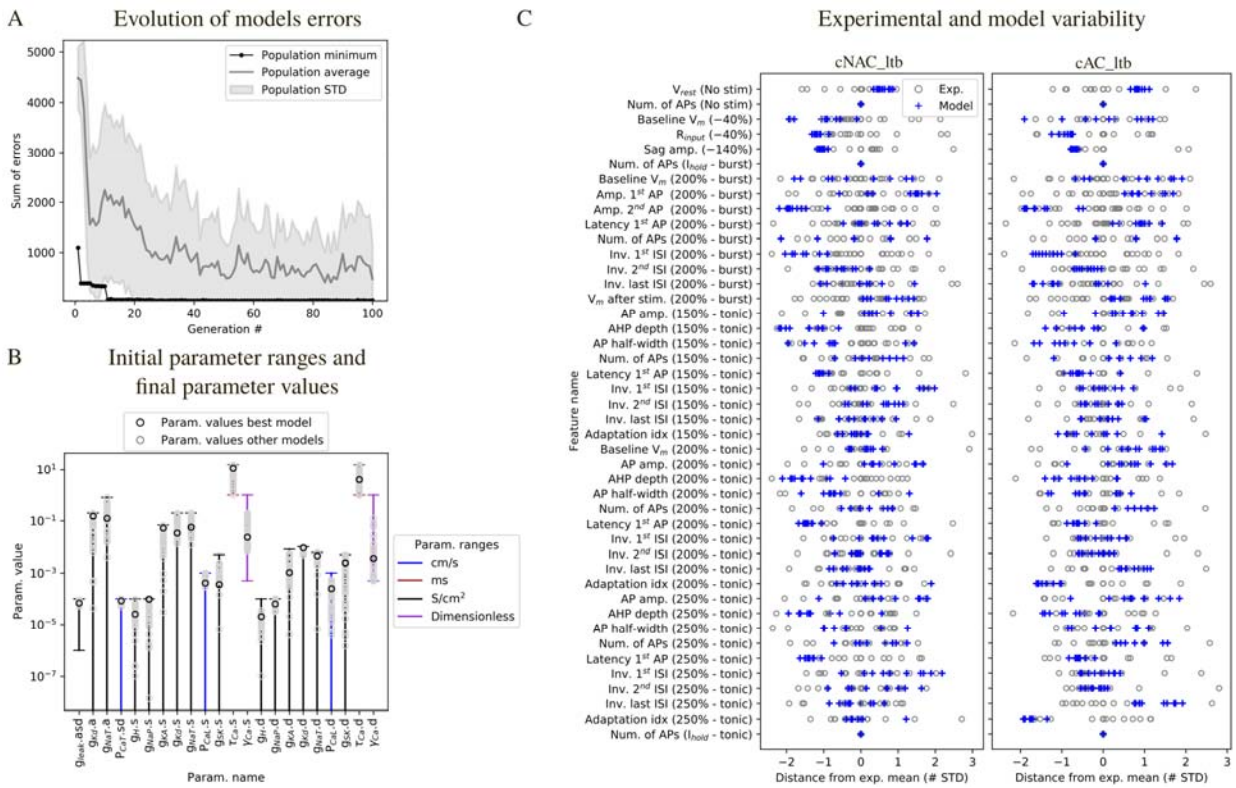


**Figure 5: Diversity of model parameters and experimental variability.**

(A) Example of model fitting errors (sum of all feature errors) during optimization. (B) Initial parameter ranges and diversity of solutions. Each vertical line represents the range for the parameters, when the horizontal lower bar is missing the bound is 0. The characters following "." in the parameter name specifies the morphological compartment for the parameter ("s": soma, "d": dendrites, "a": axon). Black circles: parameter values for one of the models in Fig 4, grey circles: parameter values of the models with all feature errors below 3 STD. (C) Features variability in the models and experiments. Blue crosses: feature errors of a sample of 10 models. Each grey circle is the z-scored feature value of one experimental cell, obtained from the feature values shown in Fig 3. The protocol names are shown in parenthesis and corresponds to the stimuli shown in Fig 1 and Fig 4, tonic and burst refer to the holding current as in Fig 1.

236

237 Spike-shape related features (e.g. AP. amplitude) in the different models covered the
238 space of the experimental variability, while for some features (e.g. input resistance, $R_{input}$), all
239 models tended to cluster on one of the tails of the experimental distribution. $R_{input}$ relates to
240 the neuron passive properties and depends both on the number of channels open at rest
241 (inverse of the leak conductance in the model) and the size of the cell. Given that all the models
242 were constrained on a single morphology, this result is not surprising. The number of action
243 potentials (Num. of APs) in different conditions (No stim, $I_{hold}$) ensured that the models did not
244 spike in the absence of a stimulus or in response to the holding current. For this reason, all the
245 experimental and model feature values in 5C are equal to 0. Other features, such as latency to
246 the first spike and sag amplitude were less variable in the models compared to experiments.
247 We hypothesized that this depended on the variable stimulation amplitudes applied to
248 different experimental cells, while all the models were stimulated with the same current
249 amplitudes.

250 We examined the diversity of the parameter values with respect to the initial parameter
251 range (Fig 5B). Most of the optimized parameter values spanned intervals larger than one order
252 of magnitude. On the other hand, some parameter values were restricted to one order of
253 magnitude, for example the permeability of the low-threshold calcium current $P_{CaT}$. This result
254 is in agreement with experiments showing a minimum value of $I_{CaT}$ is critical to generate burst
255 activity and this critical value is reached only at a certain postnatal age (27). The value of $P_{CaT}$
256 was constrained by features measuring burst activity (such as number of spikes, frequency,
257 etc.).

## Assessment of model generalization

We used different stimuli for model fitting (current steps) and for generalization assessment (current ramps and noise). We simulated the experimental ramp currents in-silico, by stimulating the models with the appropriate holding currents for the two firing modes and a linearly increasing current. We first compared visually the model responses with the experimental recordings (Fig 6A).

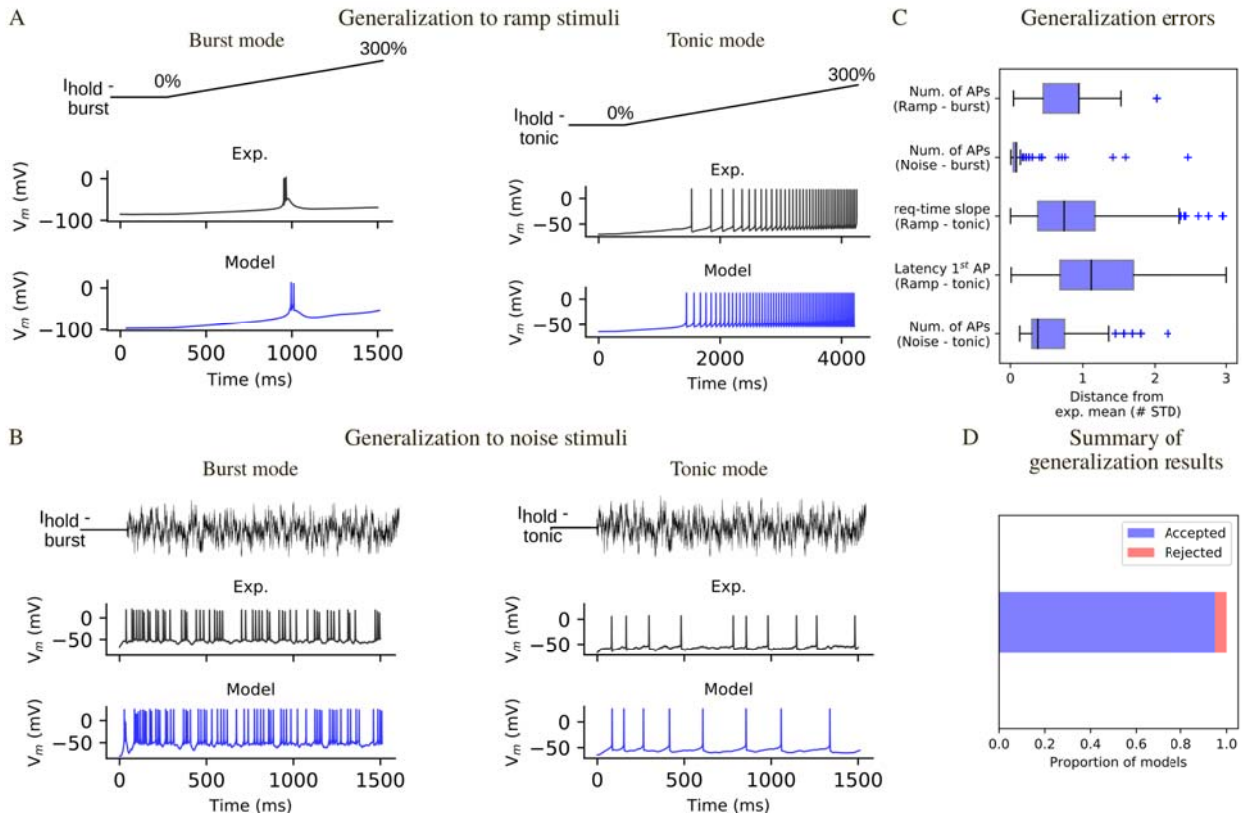


**Figure 6: Model generalization.**

(A) Responses to a ramp current injection in burst mode (left) and tonic mode (center). (B) Responses to a noise current generated according to an Ornstein-Uhlenbeck process and scaled based on the excitability of the different experimental cells and models (see Methods). (C) Generalization errors for all the models that passed the generalization test (all generalization

271 errors <3 STD). (D) Proportion of models that passed the generalization test (see Fig S4 for
272 examples of models that failed this test).
273
274 In burst mode, the models reproduced the different behaviors observed experimentally:
275 absence of a burst, small low-threshold spike, burst, burst followed by tonic firing (Fig S4).
276 Moreover, the latency of burst generation substantially overlapped with the experimental one.
277 However, a small fraction of models (1.2 %) generate repetitive burst that we have never
278 observed in the experimental recordings (Fig S4). These models were quantitatively rejected by
279 considering the number of spikes and the inter-spike intervals. In tonic mode, the latency to
280 first spike, the voltage threshold, the shape of the subsequent action potentials and the
281 increase in firing frequency were comparable with the experimental recordings (Fig 6A). In
282 addition, we quantified the generalization error to ramp stimuli (Fig 6C), by considering the
283 latency to first spike, firing frequency increase over time (tonic mode) or number of spikes
284 (burst mode).
285 Although conductance-based models can be fit by using step and ramp currents (26),
286 these stimuli are different from synaptic inputs, which can be simulated by injecting noisy
287 currents. To test the response to such network-like input, we used a noisy current varying
288 accordingly to an Ornstein-Uhlenbeck (OU) process (28) to compare models' responses with the
289 experimental data. Each experimentally recorded cell was stimulated with the same OU input,
290 scaled by a factor *w*. Experimentally, *w* was calculated during the experiment by evaluating the
291 responses to previous stimuli. We developed a similar approach to generate the noise stimuli in
292 silico (see Methods). The noise current was injected on top of the holding currents used during

293 the optimization. We found that the models reproduced well the subthreshold potential, spike
294 times and the distribution of single spikes and bursts (Fig 6B). Moreover, we quantitatively
295 evaluated the generalization to the noise stimulus by extracting features (e.g. number of spikes)
296 and comparing them with the experimental mean.

297 We computed generalization errors for each model, which were calculated similarly to
298 the optimization errors (Fig 6C). We considered a model acceptable after generalization if it had
299 all generalization errors <3 STD and we found that the majority of the models (>90%) passed
300 the generalization test.

301

302 **Sensitivity of electrical features to small parameter perturbations**

303 We assessed the robustness of the models to small changes in their parameter values. To
304 that end, we varied each parameter at a time by a small amount (± 2.5 % of the optimized
305 value) and computed the values of the features. A sensitivity value of 2 between parameter *p*
306 and feature *y* means that a 3 % change in *p* caused a 6 % change in *f*. We ranked the
307 parameters from the most to the least influential and the features from the most sensitive to
308 the least sensitive.

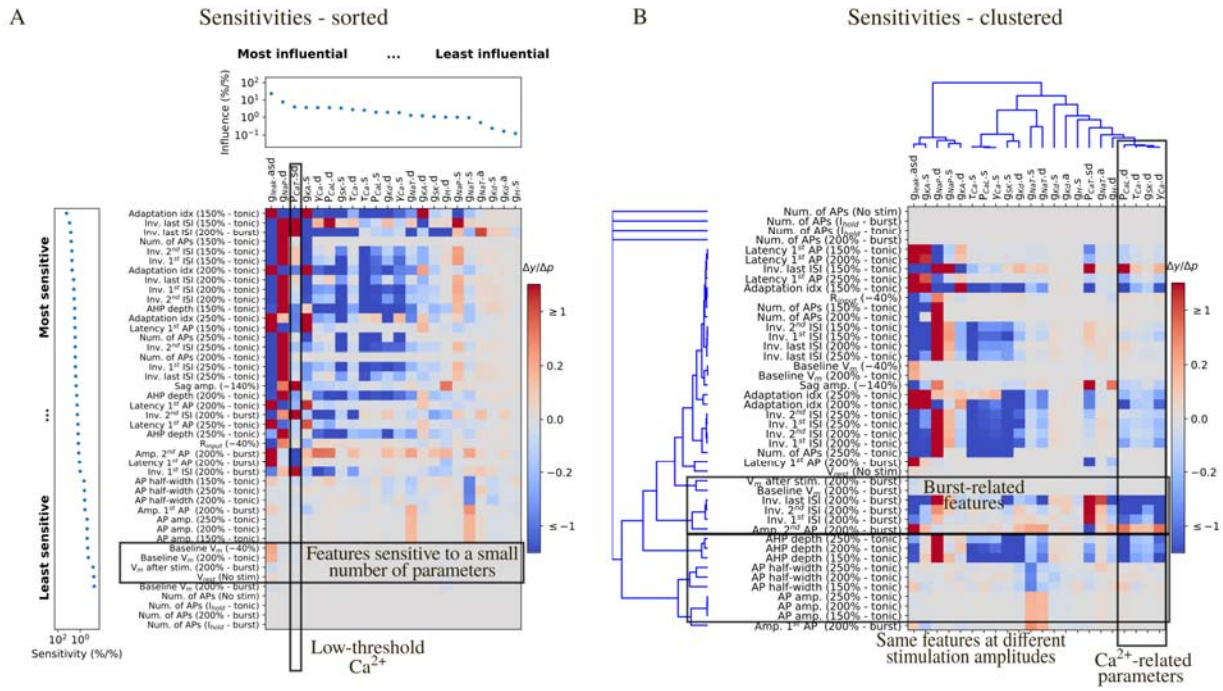


**Figure 7: Local sensitivity analysis.**

(A) Sensitivity of the feature values to small changes to the parameter values for the cAD_ltb model in Fig 4. Sensitivities (Δy/Δp) are color coded as a heat map. Features are ranked from the most to the least sensitive and parameters are ranked from the most to the least influential. The last three rows are features that ensure that the models were not firing without input or in the response to the holding current. Small changes to the parameter values are not expected to make the model firing and thus the sensitivity of these features is 0. (B) Same sensitivity values as in (a), with features and parameters clustered by similar sensitivity and influences.

The conductance of the leak current $g_{leak}$ emerged as the most influential parameter (Fig 7A). An increase in $g_{leak}$ caused a decrease in firing frequency (inverse of inter-spike intervals, ISIs) in both the tonic and burst firing modes. These results are easy to interpret when considering

Ohm's law: increasing $g_{leak}$ means decreasing the input resistance of the model, so that for the same input current the voltage response becomes smaller. The second most influential parameter was the conductance of the persistent sodium current $g_{NaP}$ in the dendrites, which increased the tonic firing rate as expected from a depolarizing current and had an effect on the late phase of the low- threshold burst (inverse last ISI - burst). An increase in the permeability of the low-threshold calcium current $P_{CaT}$, known to be one the main currents underlying low threshold bursting, enhanced burst firing responses (it decreased the inverse of ISIs) and had effects on some of the tonic features. $P_{CaT}$ was the third most influential parameter. These findings show that $I_{CaT}$ is the main driver of the low-threshold burst, but other currents, such as $I_{NaP}$ contributes as well. Increasing the dendritic permeability of the high threshold calcium current $P_{CaL}$ decreased the tonic firing rate, despite being a depolarizing current. Increasing $P_{CaL}$ means higher $Ca^{2+}$ influx and higher amplitude of the $Ca^{2+}$-activated potassium current ($I_{SK}$). The parameter $g_{SK}$ had indeed a similar effect on the features and thus clustered together with $P_{CaL}$ (Fig 7B). Increasing the conductance of the transient sodium conductance $g_{NaT}$ increased action potential amplitude and decreased its duration. Sag amplitude, that is known to depend on the activity of $I_H$, was mainly influenced by change in $g_{leak}$, $P_{CaT}$ and $g_H$. In summary, each parameter influenced at least one feature. Some features were weakly influenced by small parameter changes, e.g. baseline voltage, which depend more on the holding current amplitude, than on the model parameters. These results indicate that the model ability to generate tonic and burst firing is robust to small changes in parameter values and that all the parameters were constrained during the optimization by one or more features.

344 We then analyzed which features depended similarly on parameter changes, as they may
345 add superfluous degrees of freedom during parameters search. Fig 7B shows the same
346 sensitivities as in Fig 7A, clustered by their similarities (see Methods). Features clustered
347 together if they were sensitive to similar parameter combinations and parameters clustered
348 based on their similar influence on the features. Not surprisingly, the same tonic features
349 measured at different level of current stimulation clustered together (e.g. AP amplitude and
350 half-width, AHP depth, latency of the first ISI) and tonic firing features belonged to a cluster
351 that was different from burst features.
352

353 **Preservation of model firing properties with different morphologies**

354 We optimized the parameters for the adapting and non-adapting e-models in combination with
355 two different experimental morphologies and then tested them with the other 48
356 morphologies. Considering that morphologies could not be classified in different m-types based
357 on topological analysis of their dendrites and that TC neurons have been shown to be
358 electrically compact (15), we expected the electrical behavior to be conserved when changing
359 morphology. Nonetheless, different neurons vary in their input resistance $R_{input}$ and rheobase
360 current $I_{thr}$ due to variation in the surface area. Variation in $R_{input}$ and $I_{thr}$ made the current
361 amplitude applied during the optimization inadequate to generate the appropriate voltage
362 trajectories. We thus devised an algorithm to search for the holding current to obtain the target
363 holding voltage (for example −64 mV or −84 mV for tonic and burst firing, respectively) and $I_{thr}$
364 from the desired holding voltage. The different e-model/morphology combinations (me-
365 combinations) were evaluated by computing the same feature errors calculated during

optimization. For each morphology, we selected the e-model that generated the smallest maximum error. All me-combinations reproduced burst and tonic firing (Fig 8C). However, two me-combinations generated responses with a small number of features that deviated from the experimental mean. We chose the value of 3 STD as a threshold to define which me-combinations were acceptable (29), yielding 48 acceptable me-combinations out of the 50 tested (Fig 8A). We analyzed more closely which features were significantly different from the experimental mean. In Fig 8B we show that the rejected me-combinations had too many action potentials in the burst.

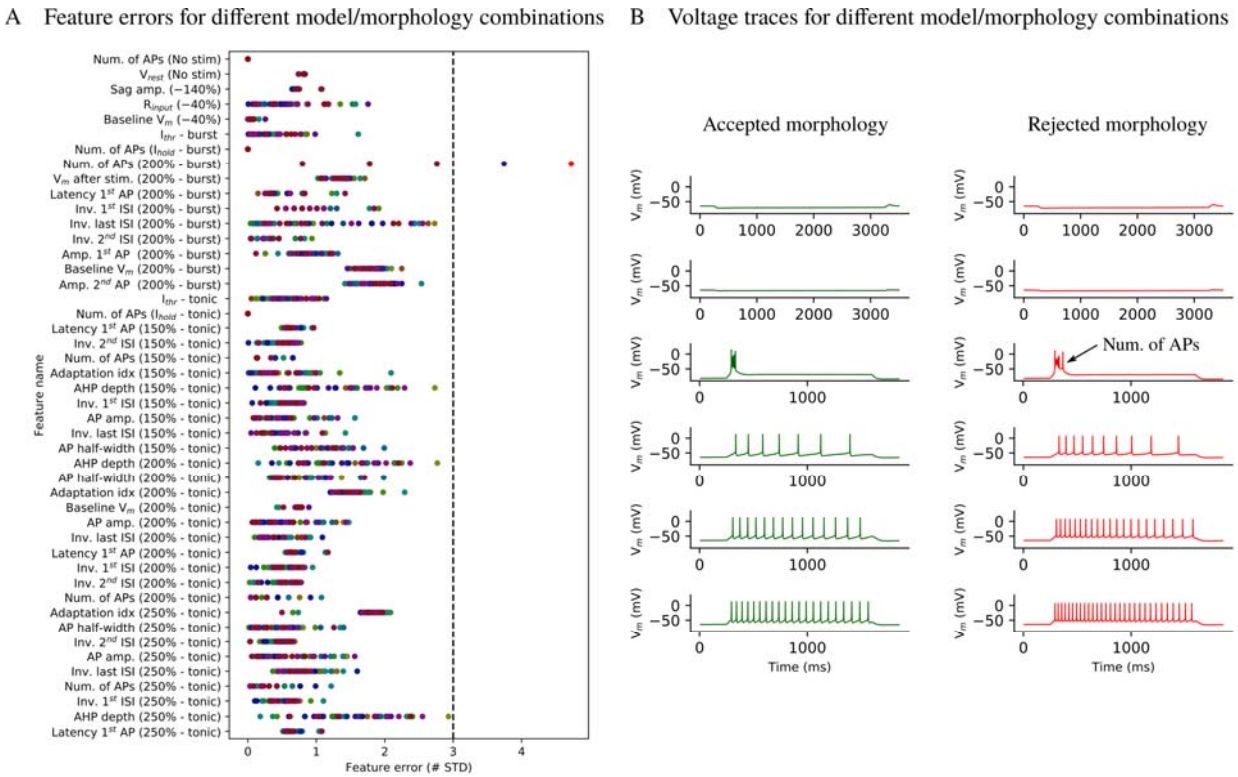


**Figure 8: Model generalization to different experimental morphologies.**

(A) Feature errors from the best electrical models (e-model) showed in Fig 4 applied to 50 different TC cell morphologies. Each morphology is represented with a different color. E-

379 models/morphology combinations with at least one feature error > 3 STD (dashed line) were
380 rejected. (B) Example of voltage responses from an accepted and from a rejected e-
381 model/morphology combination. Feature errors for the rejected combination are shown in red
382 in (A) and are indicated on the voltage trace.
383

384 **Discussion**

385 Our objective was to apply and extend an existing data-driven pipeline to identify the cell
386 types and build models of VB thalamocortical neurons that reproduce the multiple firing modes
387 that have been experimentally observed. We successfully modelled these novel firing types, by
388 including additional stimulation protocols and features to constrain the low-threshold burst.
389 Our morphological and electrical data were used to define the properties of VB TC
390 neurons in the rat. We found two electrical types (e-types) of TC neurons, but no objectively
391 different morphological types (m-types) were revealed either using Sholl analysis (21) or
392 topological analysis of dendritic branching (20). We cannot exclude that refinements to these
393 methods will reveal different m-types similar to the ones described in the visual thalamus of the
394 mouse (30). We also showed that automatic parameter search can be applied to build
395 biophysically and morphologically detailed models. This method was already applied to model
396 canonical firing behavior in cortical, hippocampal and cerebellar granule neurons
397 (9,10,16,17,31,32). To the best of our knowledge, such an automatic parameter search has not
398 previously been used to capture different firing modes and complex firing behavior such as low-
399 threshold bursting in thalamic neurons. Standardized electrophysiological protocols allowed us
400 to identify for the first time in juvenile rat adapting and non-adapting e-types of TC VB neurons

401 that were previously observed in other species (7). This finding suggests that the intrinsic
402 properties of TC neurons contribut to adaptation, a key phenomenon for filtering out irrelevant
403 stimuli, before sensory information reaches the neocortex. Further experiments are needed to
404 elucidate the relative contribution of intrinsic mechanisms and network properties to
405 adaptation in somatosensory systems. We named the two main e-types continuous non-
406 adapting low-threshold bursting (cNAD_ltb) and continuous adapting low-threshold bursting
407 (cAD_ltb) by following and extending existing conventions (16,22,31).

408 In this study, we improved upon previous morphologically and biophysically detailed
409 models of tonic and burst firing in TC neurons (12,13,15) by explicitly constraining the
410 parameters with experimental data, without hand-tuning of parameter values. Unlike previous
411 models, we chose a multi-objective optimization for a methodological and a scientific reason: it
412 is more time-efficient, reproducible, and it approximates the variability in ionic channel
413 expression of biological neurons (31,33–35), as shown by the family of acceptable solutions we
414 found. However, experiments aimed at quantifying ion channel conductances are essential to
415 assess if these solutions fall between biological ranges. Furthermore, we tested the
416 generalization capability of the models and found that more than 90% of the models were
417 comparable with the experimental data.

418 Nonetheless, we noticed some inaccuracies when comparing the voltage traces with the
419 experimental data when assessing the generalization of some models. For instance, some
420 models tended to generate small transient oscillations in response to ramp stimuli in burst
421 mode. This result is not surprising, considering that the exact kinetics for all the ionic currents
422 are not available and that there are known limitations in models of ionic channels derived from

423 the literature or from other models (36,37). In particular, modifications of the kinetics of the
424 low-threshold calcium current was shown to explain the propensity to generate oscillatory
425 bursts in TC neurons of other nuclei and species (38).

426 TC neurons have been shown to be electrically compact (15) and could, in principle, be
427 modeled as a single compartment. However, active mechanisms need to be located in the
428 dendrites in order to ensure synaptic integration and amplification (39). Information regarding
429 specific conductances or firing properties in the dendrites of TC neurons is limited. For this
430 reason, dendritic parameters in our models may be underconstrained. However, the sensitivity
431 analysis (see below) revealed that dendritic parameters did not appear to be the least
432 constrained because they influenced different tonic and burst-related features.

433 We included in the model fitting and validation pipeline a sensitivity analysis, which is
434 often neglected in computational neuroscience (40). Although we cannot use our simple
435 univariate approach to explore multidimensional parameter correlations and principles of co-
436 regulation of ion channels expression, it is useful to find better constraints for parameters
437 optimization. The selection of the features is indeed a step that still requires care and
438 experience by modelers. Furthermore, this type of sensitivity analysis allows to identify
439 parameters that can be traded-off during the optimization and that can be removed in order to
440 reduce the dimensionality of the problem. In our study, four parameters related to the calcium
441 dynamics were shown to influence the features in a very similar fashion. This type of analysis is
442 of particular importance in future work aimed at using the full diversity of ion channels that can
443 be inferred from gene expression data. More in detail, we propose that sensitivity analysis
444 should be a fundamental tool in selecting which conductances are successfully optimized by the

445 available experimental constraints. The example we showed is a local approach, applied to a
446 specific solution to the optimization problem, which showed that our models are robust to
447 small parameter changes. This analysis can be extended to study how the sensitivities vary in
448 the neighborhood of different solutions.

449 In conclusion, we systematically studied the morphological and electrical properties of VB
450 TC neurons and used these experimental data to constrain single neuron models, test their
451 generalization capability and assess their robustness. Further work will validate these models in
452 response to synaptic activity, in order to include them in a large-scale model of thalamocortical
453 microcircuitry (16).

454

455 ## Methods

456 **Experimental procedures**

457 Experimental data were collected in conformity with the Swiss Welfare Act and the Swiss
458 National Institutional Guidelines on Animal Experimentation for the ethical use of animals. The
459 Swiss Cantonal Veterinary Office approved the project following an ethical review by the State
460 Committee for Animal Experimentation.

461 All the experiments were conducted on coronal or horizontal brain slices (300 µm thick-
462 ness) from the right hemisphere of male and female juvenile (P14-18) Wistar Han rats. The
463 region of interest was identified using the Paxinos and Watson rat brain atlas (19). After
464 decapitation, brains were quickly dissected and sliced (HR2 vibratome, Sigmann Elektronik,
465 Germany) in ice-cold standard ACSF (in mM: NaCl 125.0, KCl 2.50, $MgCl_2$ 1.00, $NaH_2PO_4$ 1.25,

466 $CaCl_2$ 2.00, D-(+)-Glucose 50.00, $NaHCO_3$ 50.00; pH 7.40, aerated with 95% $O_2$ / 5% $CO_2$).
467 Recordings of thalamocortical neurons in the VB complex were performed at 34 °C in standard
468 ACSF with an Axon Instruments Axopatch 200B Amplifier (Molecular Devices, USA) using 5–7
469 MΩ borosilicate pipettes, containing (in mM): $K^+$-gluconate 110.00, KCl 10.00, ATP-$Mg^{2+}$ 4.00,
470 $Na_2$-phosphocreatine 10.00, GTP-$Na^+$ 0.30, HEPES 10.00, biocytin 13.00; pH adjusted to 7.20
471 with KOH, osmolarity 270-300 mOsm. Cells were visualized using infrared differential
472 interference contrast video microscopy (VX55 camera, Till Photonics, Germany and BX51WI
473 microscope, Olympus, Japan).

474 Membrane potentials were sampled at 10 kHz using an ITC-18 digitizing board
475 (InstruTECH, USA) controlled by custom-written software operating within IGOR Pro
476 (Wavemetrics, USA). Voltage signals were low-pass filtered (Bessel, 10 kHz) and corrected after
477 acquisition for the liquid junction potential (LJP) of −14 mV. Only cells with a series resistance
478 <25 MΩ were used.

479 After reaching the whole-cell configuration, a battery of current stimuli was injected into
480 the cells and repeated 2-4 times (e-code). During the entire protocol, we defined offset
481 currents in order to keep the cell at −50 mV (tonic firing) or −70 mV (burst firing) before LJP
482 correction and applied them during the entire protocol. The step and ramp currents were
483 injected with a delay of 250 ms in the experiment. In the models, the stimuli were injected with
484 a delay of 800 ms, to allow for the decay of transients due to initialization. Each stimulus was
485 normalized to the rheobase current of each cell, calculated on-line as the current that elicited
486 one spike (stimulus TestAmp, duration 1350 ms). The stimuli used for in the experiments, for
487 fitting and testing the models were:

488 • IDRest: current step of 1350 ms, injected at different amplitude levels in 25 %
489 increments (range 50-300 % threshold). IDRest was renamed to Step in the model.
490 • IDThresh: current step with duration of 270 ms, 4 % increments (range 50 - 130 %).
491 • IV: hyperpolarizing and depolarizing steps of 3000 ms injected in 20 % increments (range
492 −140 - 60%).
493 • SponNoHold: the first 10 seconds of this stimulus was used to calculate the resting
494 membrane potential. No holding or stimulation currents were applied.
495 • SponHold: the first 10 seconds of this stimulus was used to calculate the holding current
496 applied to keep the cells at the target potential.
497 • PosCheops: ramps of current from 0 to 300 % and from 300 to 0 % having progressively
498 shorter durations (4000 ms, 2000 ms, 1250 ms). To test the models in tonic mode we
499 used the first increasing ramp in the stimulus, while we used the last one in the bursting
500 firing mode. We chose the last one because the biological cells were more likely to
501 generate a burst.
502 • NOISEOU3: the original wave was scaled and offset for each cell based on the spike
503 frequency responses to IDRest responses. The scaling factor *w* was extracted from the
504 frequency-current curve and corresponded to the current value that made the cell fire
505 at 7.5 Hz.

506 Neurons that were completely stained and those with high contrast were reconstructed
507 in 3D and corrected for shrinkage as previously described (41). Reconstruction used the
508 Neurolucida system (MicroBrightField). The location of the stained cells was defined by

509 overlaying the stained slice and applying manually an affine transformation to the Paxinos and
510 Watson's rat atlas (19).

511 **Electrical features extraction**

512 Electrical features were extracted using the Electrophys Feature Extraction Library (eFEL)
513 (42). We calculated the adaptation index (AI) from recordings in tonic mode (Step 200 %
514 threshold) and classified TC VB neurons into adapting (AI>=0.029) and non-adapting (AI<0.029)
515 electrical types. AI was calculated using the eFEL feature *adaptation_index2* and corresponded
516 to the average of the difference between two consecutive inter-spike intervals (ISI) normalized
517 by their sum. The cut-off value was calculated after fitting a Gaussian mixture model to the
518 bimodal data, using available routines for R (43,44). In order to group data from different cells
519 and generate population features, we normalized all the stimuli by the rheobase current $I_{thr}$ of
520 each cell. To calculate $I_{thr}$, we used IDRest and IDThresh and selected the minimal amplitude
521 that evoked a single spike. The extracted features quantified passive (input resistance, resting
522 membrane potential), burst and tonic firing properties (number of spikes, inverse of inter-spike
523 intervals, latency to first spike), action potentials shape (amplitude, half-width, depth of the fast
524 after-hyperpolarization). We aimed at finding the minimal set of features that capture the most
525 important properties. This set was a trade-off between comprehensively describing the
526 experimental data (i.e. extracting all possible features), which can lead to over-fitting and loss
527 of generalizability, and a too small set that would miss some important characteristics. For the
528 tonic firing responses, we used three stimulation amplitudes (150 %, 200 %, 250 % of firing
529 threshold) which have been shown to reproduce the complete input-output function of the
530 neurons (17,41). Responses to two hyperpolarizing steps of different amplitudes (−40 % and

531 −140 % threshold) constrained the input resistance and the conductance of currents activated
532 in hyperpolarization (*sag_amplitude* feature). We included baseline voltage values in the
533 optimization objectives to ensure that the model was in the right firing regime and spike count
534 to penalize models that were firing in response to the holding currents. Along with the voltage
535 features, we extracted mean holding and threshold current values for all the experimental
536 stimuli. Description of the features and the details on their calculation are available on-line [49].
537 Current stimuli applied during the optimization and generalization were directly obtained from
538 the experimental values or automatically calculated by following the experimental procedures
539 (e.g. noise stimulus).

540 **Morphology analysis**

541 Reconstructed morphologies were analyzed to objectively identify different
542 morphological types. The Sholl profiles of each pair of cells was statistically tested by using k-
543 samples Anderson-Darling statistics. This test was preferred to the most common Kolmogorov-
544 Smirnov test, because it does not assume that the samples are drawn from a continuous
545 distribution. The different Sholl profiles are indeed an analysis of the intersections with discrete
546 spheres.

547 To compare the topological description of each morphology we transformed the
548 persistence barcodes into persistence images and calculated their distances as in (20). Briefly,
549 we converted the persistence barcode, which encodes the start and end radial distances of a
550 branch in the neuronal tree, into a persistence diagram. In the persistence diagram, each bar of
551 the barcode is converted into a point in a 2D space, where the X and Y coordinates are the start
552 and end radial distances of each bar. The persistence diagram was then converted in a

553 persistence image by applying a Gaussian kernel. We used the library NeuroM (45) to perform
554 Sholl and morphometrics analyses. The reconstructed morphologies will be made publicly
555 available on neuromorpho.org.

556 **Ionic currents models**

557 We used Hodgkin-Huxley types of ionic current models, starting from kinetics equations
558 already available in the neuroscientific literature. Along with kinetics of the ionic currents, we
559 stored information on the experimental conditions, such as temperature and LJP, by using the
560 software NeuroCurator (46). Whenever the data was available, we compared simulated
561 voltage-clamp experiments to experimental data from juvenile rats. Ionic currents $I_i$ were
562 defined as functions of the membrane potential $v$, its maximal conductance density $g_i$ and the
563 constant value of the reversal potential $E_i$:

$$I_i = g_i\, m_i^x\, h_i^y\, (v - E_i)$$

564 $m_{ion}$ and $h_{ion}$ represent activation and inactivation probability (varying between 0 and 1), with
565 integer exponents $x$ and $y$. Each probability varied according to:

$$n'(v) = (n_\infty(v) - n)/\tau_n(v)$$

566 where $n_\infty(v)$ is a function of voltage that represents the steady-state activation/inactivation
567 function (normally fitted with a Boltzmann curve) and $\tau_n(v)$ is a voltage-dependent time
568 constant. Exceptions to this formalism are ionic currents that do not inactivate (y = 0) and ionic
569 currents with (in)activation processes mediated by two or more time constants. Calcium
570 currents ($I_{CaT}$ and $I_{CaL}$) were modeled according to the Goldman-Hodgkin-Katz constant field
571 equation and had permeability values instead of conductance (47).

572 **Fast transient sodium current $I_{NaT}$ and delayed potassium current $I_{Kd}$.** $I_{NaT}$ and $I_{Kd}$ were
573 taken from a previous models of rat TC neurons from the VB nucleus (12), available on
574 SenseLab ModelDB (accession no. 279). $I_{NaT}$ was compared with recordings of transient sodium
575 currents in P7-11 rat neurons from the dorsolateral geniculate (dLGN) nucleus (48).

576 **Low-threshold activated (T-type) calcium current $I_{CaT}$.** $I_{CaT}$ model was taken from (12) and
577 available on-line (ModelDB, accession no. 279). This model was based on data recorded from
578 VB neurons of Sprague-Dawley rats (P7-12) at room temperature and corrected for −9 mV LJP
579 (11).

580 **Hyperpolarization-activated cationic current $I_H$.** The steady-state activation for $I_H$ was
581 derived from VB thalamic neurons in P10-20 Long-Evans rats and was already corrected for −10
582 mV LJP in the original publication (49). The equation used was:

$$m_\infty = 1/(1 + \exp[(v + 86.4)/11.2])$$

583 The time constant of activation was modeled as in (50), which derived a mathematical
584 description of $I_H$ based on data from the dLGN in adult guinea pigs, recorded at 35.5 °C (51). The
585 equation describing the time dependence of activation was not corrected for simulations at
586 different temperatures and was:

$$\tau_m = 1/[\exp(-14.59 - 0.086v) + exp(-1.87 + 0.0701v)]$$

587 The equilibrium potential of the channel $E_H$ was −43 mV. In silico voltage-clamp
588 experiments were compared with data in (49).

589 **Persistent sodium current $I_{NaP}$.** We modeled $I_{NaP}$ as in (17) which based their model on
590 recordings from entorhinal neurons of Long-Evans rats (P25-P35) (52). The steady-state
591 activation was modified according to (48) and the steady-state inactivation according to (14).

592 The original steady-state activation data were recorded at room temperature (22-24°) and
593 corrected for −6/−7 mV LJP. Limited data on $I_{NaP}$ are available from dissociated neurons from
594 the dLGN nucleus in Wistar rats (48).

595 **Fast transient (A-type) potassium current $I_{KA}$.** The mathematical formulation of $I_{KA}$ was
596 based on data recorded from VB neurons in Sprague-Dawley rats (P7-15), recorded at room
597 temperature (22-24 °C) (53). A $Q_{10}$ = 2.8 was experimentally determined and used for
598 simulations at different temperatures. In the original experiments a small LJP (<−4 mV) was
599 measured and not corrected. The current had a rapid and a slow component, represented by
600 two activation and two inactivation variables. The model of this current was provided by the
601 authors of (14).

602 **High-threshold (L-type) calcium current $I_{CaL}$.** $I_{CaL}$ model is the same as TC neurons model
603 previously published (14,50). The model was based on data from isolated guinea-pig
604 hippocampal neurons, recorded at room temperature (20-22 °C) with modifications to the
605 Boltzmann curve parameters of activation contained in the correction to the original models
606 [59]. A small LJP (<3 mV) was not corrected (50). A $Q_{10}$ = 3 was used for simulations at different
607 temperatures.

608 **Calcium-activated potassium currents.** TC neuron express genes for BK-type (54) and SK-
609 type calcium-activated potassium channels (55). Models of BK-type currents, similar to the $I_C$
610 current, have already been used to model TC neurons (14,50,54). However, data characterizing
611 this current in mammalian neurons are not available. We thus included only a model of $I_{SK}$
612 (available in ModelDB, accession no. 139653) based on rat mRNA expression data in Xenopus
613 oocytes (56).

614 **Intracellular calcium dynamics.** A simple exponential decay mechanism was used to
615 model the intracellular calcium dynamics (ModelDB, accession no. 139653). Both $I_{CaT}$ and $I_{CaL}$
616 contributed to the intracellular calcium concentration.

617 In addition, we included a voltage-insensitive membrane current $I_{leak}$. The equilibrium
618 potential was −79 mV and corresponded to the average resting potential from our experimental
619 recordings.

620 **Simulation and parameters optimization**

621 NEURON 7.5 software was used for simulation (57). We used NEURON variable time step
622 method for all simulations. For the sake of spatial discretization, each section was divided into
623 segments of 40 µm length. The following global parameters were set: initial simulation voltage
624 (−79 mV), simulation temperature (34 °C), specific membrane capacitance (1 µF/cm$^2$), specific
625 intracellular resistivity 100 Ωcm for all the sections, equilibrium potentials for sodium and
626 potassium were 50 mV and −90 mV, respectively.

627 BluePyOpt (18) with Indicator Based Evolutionary Algorithm (IBEA) were used to fit the
628 models to the experimental data. Each optimization run was repeated with three different
629 random seeds and evaluated 100 individuals for 100 generations. The evaluation of these 300
630 individuals for 100 generations was parallelized using the *iPython ipyparallel* package and took
631 between 21 and 52 h on 48 CPU cores (Intel Xeon 2.60 GHz) on a computing cluster. Each
632 optimization run typically resulted in tens or hundreds of unique acceptable solutions, defined
633 as models having all feature errors below 3 STD from the experimental mean.

634 The models will be made publicly available at ModelDB (58). The configuration files for
635 the optimization and analysis will be made publicly available on Github, Bluepyopt page (59).

**Sensitivity analysis**

We performed a sensitivity analysis of an optimization solution by varying one parameter value ($p_m$) at a time and calculating the electrical features from the voltage traces ($y^+$ and $y^-$). We defined the sensitivity as the ratio between the normalized feature change and the parameter change, which for smooth functions approximates a partial derivative (60,61). The features changes were normalized by the optimized feature value. For small changes of parameter values, we assumed that the features depend linearly on its parameters. We could thus linearize the relationship between the features and the parameters around an optimized parameter set and calculate the derivatives. The derivatives were calculated with a central difference scheme (60).

$$\frac{\partial y_n}{\partial p_m} \approx \frac{y_n^+ - y_n^-}{2\Delta p_m}$$

We collected the derivatives (sensitivities) in the *N X M* Jacobian matrix, with *N* representing the number of features and *M* the number of parameters.

To rank parameters and features we computed their relative importance by calculating their norms (the square root of the summed squared values) from the Jacobian columns and rows, respectively. To cluster parameters based on similar influences on the features and to cluster features that were similarly dependent on the parameters, we used angles between columns (or rows) to compute distances *D* between parameters (or features):

$$D = 1 - |\cos\theta|$$

Features where thus considered similar if they depended in a similar manner on the parameters, independent of sign or magnitude.

## Acknowledgements

We thank the Blue Brain Project Visualization Team for generating the meshes and visualizing the 3D morphologies.

## Author Contributions

**Conceptualization**: E.I., S.L.H. **Data Acquisition and Curation:** J.Y., Y.S. **Formal Analysis**: E.I., J.Y., B.Z., C.O. **Funding Acquisition**: S.L.H., H.M. **Investigation**: E.I., J.Y., Y.S. **Methodology**: E.I., B.Z., C.R., W.V. **Project Administration:** C.O., S.L.H., H.M. **Resources and Software**: J.Y., Y.S., B.Z., W.V., C.R. **Supervision**: S.L.H., H.M. **Validation and Visualization**: E.I. **Writing – Original Draft Preparation**: E.I. **Writing – Review & Editing**: E.I., J.Y., C.O., W.V., H.M., S.L.H.

## Supporting Information captions

**S1 Features Dataset – Electrical features**

Spreadsheet containing experimental electrical figures, separated in three different sheets. The features, their means and standard deviations are used in Fig 1C, Fig 2, Fig 3, Fig 4C, Fig 5C, Fig 8A.

**S2 Supporting figures**

671 **References**


672 1. Sherman SM. The thalamus is more than just a relay. Current opinion in neurobiology.
673 2007;17(4):417–422.

674 2. Francis JT, Xu S, Chapin JK. Proprioceptive and cutaneous representations in the rat ventral
675 posterolateral thalamus. Journal of neurophysiology. 2008;99(5):2291–2304.

676 3. Jones E. The thalamus 2nd ed. Cambridge University Press Cambridge, UK; 2007.

677 4. McAlliser J, Wells J. The structural organization of the ventral posterolateral nucleus in the
678 rat. Journal of Comparative Neurology. 1981;197(2):271–301.

679 5. Llinás R, Jahnsen H. Electrophysiology of mammalian thalamic neurones in vitro. Nature.
680 1982;297(5865):406.

681 6. Jahnsen H, Llinas R. Electrophysiological properties of guinea-pig thalamic neurones: an in
682 vitro study. The Journal of physiology. 1984;349(1):205–226.

683 7. Turner JP, Anderson CM, Williams SR, Crunelli V. Morphology and membrane properties of
684 neurones in the cat ventrobasal thalamus in vitro. The Journal of Physiology.
685 1997;505(3):707–726.

686 8. Connelly WM, Crunelli V, Errington AC. Variable action potential backpropagation during
687 tonic firing and low-threshold spike bursts in thalamocortical but not thalamic reticular
688 nucleus neurons. Journal of Neuroscience. 2017;0015–17.

689 9. Druckmann S, Banitt Y, Gidon AA, Schürmann F, Markram H, Segev I. A novel multiple
690 objective optimization framework for constraining conductance-based neuron models by
691 experimental data. Frontiers in neuroscience. 2007;1:1.

692 10. Gouwens NW, Berg J, Feng D, Sorensen SA, Zeng H, Hawrylycz MJ, et al. Systematic
693 generation of biophysically detailed models for diverse cortical neuron types. Nature
694 communications. 2018;9(1):710.

695 11. Huguenard JR, McCormick DA. Simulation of the currents involved in rhythmic oscillations in
696 thalamic relay neurons. Journal of neurophysiology. 1992;68(4):1373–1383.

697 12. Destexhe A, Neubig M, Ulrich D, Huguenard J. Dendritic low-threshold calcium currents in
698 thalamic relay cells. Journal of Neuroscience. 1998;18(10):3574–3588.

699 13. Rhodes PA, Llinás R. A model of thalamocortical relay cells. The Journal of physiology.
700 2005;565(3):765–781.

701 14. Amarillo Y, Zagha E, Mato G, Rudy B, Nadal MS. The interplay of seven subthreshold
702 conductances controls the resting membrane potential and the oscillatory behavior of
703 thalamocortical neurons. Journal of Neurophysiology. 2014;112(2):393–410.

704 15. Connelly WM, Crunelli V, Errington AC. The global spike: conserved dendritic properties
705 enable unique Ca2+ spike generation in low-threshold spiking neurons. Journal of
706 Neuroscience. 2015;35(47):15505–15522.

707 16. Markram H, Muller E, Ramaswamy S, Reimann MW, Abdellah M, Sanchez CA, et al.
708 Reconstruction and Simulation of Neocortical Microcircuitry. Cell. 2015;163(2):456–492.

709 17. Hay E, Hill S, Schürmann F, Markram H, Segev I. Models of neocortical layer 5b pyramidal
710 cells capturing a wide range of dendritic and perisomatic active properties. PLoS
711 computational biology. 2011;7(7):e1002107.

712 18. Van Geit W, Gevaert M, Chindemi G, Rössert C, Courcol J-D, Muller EB, et al. BluePyOpt:
713 leveraging open source software and cloud infrastructure to optimise model parameters in
714 neuroscience. Frontiers in neuroinformatics. 2016;10:17.

715 19. Paxinos G, Watson C. The rat brain atlas in stereotaxic coordinates. San Diego: Academic.
716 1998;

717 20. Kanari L, D\lotko P, Scolamiero M, Levi R, Shillcock J, Hess K, et al. A topological
718 representation of branching neuronal morphologies. Neuroinformatics. 2018;16(1):3–13.

719 21. Sholl DA. Dendritic organization in the neurons of the visual and motor cortices of the cat.
720 Journal of anatomy. 1953;87(Pt 4):387.

721 22. Ascoli G a, Alonso-Nanclares L, Anderson S a, Barrionuevo G, Benavides-Piccione R,
722 Burkhalter A, et al. Petilla terminology: nomenclature of features of GABAergic
723 interneurons of the cerebral cortex. Nature reviews Neuroscience. 2008;9(7):557–568.

724 23. Almog M, Korngreen A. Is realistic neuronal modeling realistic? Journal of neurophysiology.
725 2016;116(5):2180–2209.

726 24. Williams SR, Stuart GJ. Action potential backpropagation and somato-dendritic distribution
727 of ion channels in thalamocortical neurons. Journal of Neuroscience. 2000;20(4):1307–
728 1317.

729 25. Errington AC, Renger JJ, Uebele VN, Crunelli V. State-dependent firing determines intrinsic
730 dendritic Ca2+ signaling in thalamocortical neurons. Journal of Neuroscience.
731 2010;30(44):14843–14853.

732 26. Druckmann S, Berger TK, Hill S, Schürmann F, Markram H, Segev I. Evaluating automated
733 parameter constraining procedures of neuron models by experimental and surrogate data.
734 Biological cybernetics. 2008;99(4–5):371.

735 27. Velazquez JLP, Carlen PL. Development of firing patterns and electrical properties in
736 neurons of the rat ventrobasal thalamus. Developmental brain research. 1996;91(2):164–
737 170.

738 28. Pozzorini C, Mensi S, Hagens O, Naud R, Koch C, Gerstner W. Automated high-throughput
739 characterization of single neurons by means of simplified spiking models. PLoS
740 computational biology. 2015;11(6):e1004275.

741 29. Hay E, Schürmann F, Markram H, Segev I. Preserving axosomatic spiking features despite
742 diverse dendritic morphology. Journal of neurophysiology. 2013;109(12):2972–2981.

743 30. Krahe TE, El-Danaf RN, Dilger EK, Henderson SC, Guido W. Morphologically distinct classes
744 of relay cells exhibit regional preferences in the dorsal lateral geniculate nucleus of the
745 mouse. Journal of Neuroscience. 2011;31(48):17437–17448.

746 31. Migliore R, Lupascu CA, Bologna LL, Romani A, Courcol J-D, Antonel S, et al. The
747 physiological variability of channel density in hippocampal CA1 pyramidal cells and
748 interneurons explored using a unified data-driven modeling workflow. PLoS computational
749 biology. 2018;14(9):e1006423.

750 32. Masoli S, Rizza MF, Sgritta M, Van Geit W, Schürmann F, D'Angelo E. Single neuron
751 optimization as a basis for accurate biophysical modeling: the case of cerebellar granule
752 cells. Frontiers in cellular neuroscience. 2017;11:71.

753 33. Schulz DJ, Goaillard J-M, Marder E. Variable channel expression in identified single and
754 electrically coupled neurons in different animals. Nature neuroscience. 2006;9(3):356.

755 34. Taylor AL, Goaillard J-M, Marder E. How multiple conductances determine
756 electrophysiological properties in a multicompartment model. Journal of Neuroscience.
757 2009;29(17):5573–5586.

758 35. O'Leary T, Williams AH, Caplan JS, Marder E. Correlations in ion channel expression emerge
759 from homeostatic tuning rules. Proceedings of the National Academy of Sciences.
760 2013;110(28):E2645–E2654.

761 36. Ranjan R, Khazen G, Gambazzi L, Ramaswamy S, Hill SL, Schürmann F, et al. Channelpedia:
762 an integrative and interactive database for ion channels. Frontiers in neuroinformatics.
763 2011;5:36.

764 37. Podlaski WF, Seeholzer A, Groschner LN, Miesenböck G, Ranjan R, Vogels TP. Mapping the
765 function of neuronal ion channels in model and experiment. Elife. 2017;6:e22152.

766 38. Wei H, Bonjean M, Petry HM, Sejnowski TJ, Bickford ME. Thalamic burst firing propensity: a
767 comparison of the dorsal lateral geniculate and pulvinar nuclei in the tree shrew. Journal of
768 Neuroscience. 2011;31(47):17287–17299.

769 39. Connelly WM, Crunelli V, Errington AC. Passive synaptic normalization and input synchrony-
770 dependent amplification of cortical feedback in thalamocortical neuron dendrites. Journal
771 of Neuroscience. 2016;36(13):3735–3754.

772 40. Tennøe S, Halnes G, Einevoll GT. Uncertainpy: A Python toolbox for uncertainty
773 quantification and sensitivity analysis in computational neuroscience. bioRxiv. 2018;274779.

774 41. Markram H, Muller E, Ramaswamy S, Reimann MW, Abdellah M, Sanchez CA, et al.
775 Reconstruction and simulation of neocortical microcircuitry. Cell. 2015;163(2):456–492.

776 42. BlueBrain. BlueBrain/eFEL [Internet]. 2018. Available from:
777 https://github.com/BlueBrain/eFEL

778 43. RStudio Team. RStudio: Integrated Development Environment for R [Internet]. Boston, MA:
779 RStudio, Inc.; 2016. Available from: http://www.rstudio.com/

780 44. Choisy M. Identifying a cutoff value from bimodal data [Internet]. 2018. Available from:
781 http://marcchoisy.free.fr/fmm/index.html

782 45. BlueBrain. BlueBrain/NeuroM [Internet]. 2018. Available from:
783 https://github.com/BlueBrain/NeuroM

784 46. O'Reilly C, Iavarone E, Hill SL. A Framework for Collaborative Curation of Neuroscientific
785 Literature. Frontiers in neuroinformatics. 2017;11:27.

786 47. Hille B. Ionic channels in excitable membranes. Current problems and biophysical
787 approaches. Biophysical Journal. 1978;22(2):283–294.

788 48. Parri HR, Crunelli V. Sodium current in rat and cat thalamocortical neurons: role of a non-
789 inactivating component in tonic and burst firing. Journal of Neuroscience. 1998;18(3):854–
790 867.

791 49. Budde T, Biella G, Munsch T, Pape H-C. Lack of Regulation by Intracellular Ca2+ of the Hyper
792 Polarization-Activated Cation Current in Rat Thalamic Neurones. The Journal of physiology.
793 1997;503(1):79–85.

794 50. McCormick D a, Huguenard JR. A model of the electrophysiological properties of
795 thalamocortical relay neurons. Journal of neurophysiology. 1992;68(4):1384–1400.

796 51. McCORMICK DA, Pape H-C. Properties of a hyperpolarization-activated cation current and
797 its role in rhythmic oscillation in thalamic relay neurones. The Journal of physiology.
798 1990;431(1):291–318.

799 52. Magistretti J, Alonso A. Biophysical properties and slow voltage-dependent inactivation of a
800 sustained sodium current in entorhinal cortex layer-II principal neurons: a whole-cell and
801 single-channel study. The Journal of general physiology. 1999;114(4):491–509.

802 53. Huguenard J, Coulter D, Prince D. A fast transient potassium current in thalamic relay
803 neurons: kinetics of activation and inactivation. Journal of neurophysiology.
804 1991;66(4):1304–1315.

805 54. Ehling P, Cerina M, Meuth P, Kanyshkova T, Bista P, Coulon P, et al. Ca2+-dependent large
806 conductance K+ currents in thalamocortical relay neurons of different rat strains. Pflügers
807 Archiv-European Journal of Physiology. 2013;465(4):469–480.

808 55. Gymnopoulos M, Cingolani LA, Pedarzani P, Stocker M. Developmental mapping of small-
809 conductance calcium-activated potassium channel expression in the rat nervous system.
810 Journal of Comparative Neurology. 2014;522(5):1072–1101.

811 56. Köhler M, Hirschberg B, Bond C, Kinzie JM, Marrion N, Maylie J, et al. Small-conductance,
812 calcium-activated potassium channels from mammalian brain. Science.
813 1996;273(5282):1709–1714.

814 57. Hines ML, Carnevale NT. The NEURON simulation environment. Neural computation.
815 1997;9(6):1179–1209.

816 58. McDougal RA, Morse TM, Carnevale T, Marenco L, Wang R, Migliore M, et al. Twenty years
817 of ModelDB and beyond: building essential modeling tools for the future of neuroscience. J
818 Comput Neurosci. 2017 Feb 1;42(1):1–10.

819 59. BlueBrain. BlueBrain/BluePyOpt [Internet]. 2018. Available from:
820 https://github.com/BlueBrain/BluePyOpt

821 60. Weaver CM, Wearne SL. Neuronal firing sensitivity to morphologic and active membrane
822 parameters. PLoS Computational Biology. 2008;4(1):e11.

823 61. Olifer AV. Neuronal Parameter Sensitivity. In: Jaeger D, Jung R, editors. Encyclopedia of
824 Computational Neuroscience [Internet]. New York, NY: Springer New York; 2013 [cited 2018
825 Dec 19]. p. 1–6. Available from: https://doi.org/10.1007/978-1-4614-7320-6_172-1

826